

Model-Free Coordinated Optimization of IBR Controllers for Enhanced Grid-Level Transient Dynamic Performance

Haowen Xu and Xin Chen

Abstract—With the increasing penetration of inverter-based resources (IBRs) in power grids, system-level coordinated optimization of IBR controllers has become increasingly important for maintaining overall system stability. Unlike most existing methods that rely on simplified or linearized dynamic models and focus on small-signal stability or isolated tuning of individual facilities, this paper proposes a novel simulation-based, model-free framework for the coordinated optimization of IBR control parameters to enhance grid transient dynamic performance. The framework uses a high-fidelity power system simulator to accurately evaluate grid transient dynamic responses, and a projected multi-point zeroth-order optimization algorithm with adaptive moment estimation, termed PMZO-Adam, is proposed to solve the problem in a model-free manner, thus eliminating the need for explicit mathematical models of complex nonlinear system dynamics. The proposed framework enables direct optimization of grid transient dynamic behavior and system-wide coordinated tuning of IBR controllers. Extensive simulations demonstrate the effectiveness of the proposed approach in optimizing IBR control parameters to improve grid transient frequency response under large disturbances.

Index Terms—Control parameter tuning, zeroth-order methods, model-free optimization, transient dynamic performance.

I. INTRODUCTION

The electric power grid is undergoing a profound transformation driven by the increasing integration of inverter-based resources (IBRs), such as wind turbines, solar panels, and battery energy storage systems. Unlike conventional synchronous generators with large rotating masses [1], IBRs interface with the grid through power electronic inverters. Consequently, power systems with high IBR penetration exhibit fundamentally different dynamic behaviors, reduced system inertia, and increased challenges for maintaining grid stability [2]. The dynamics of IBRs are primarily governed by their control strategies, which are broadly categorized as grid-forming (GFM) and grid-following (GFL) controls [3]. As IBRs are interconnected through the power network, effective grid-level coordination of GFM and GFL controllers becomes essential for maintaining overall system stability and enhancing transient performance.

Traditionally, IBR control settings and parameters are determined empirically by the original equipment manufacturer or facility operator, based on operational experience and tuned independently at the device level [4]. A number of studies have applied control-theoretic methods, such as eigenvalue analysis, root locus, and small-signal modeling

[5]–[7], and model-based optimization approaches [8]–[10], to derive optimal controller parameter settings. However, these model-based methods typically rely on simplified or linearized system dynamic models and primarily focus on small-signal stability, which may fail to capture the nonlinear dynamics of practical systems and can lead to suboptimal or even unstable performance under large disturbances [11].

To overcome the limitations of model-based methods, data-driven techniques have been explored, including reinforcement learning [12], [13] and meta-heuristic algorithms, such as particle swarm optimization and genetic algorithms [14], [15]. Nevertheless, these data-driven approaches generally lack performance guarantees, raising concerns about their optimality and reliability. Furthermore, many existing studies focus on optimizing the parameters of an individual IBR independently [16], [17]. Such localized facility-level control parameter tuning overlooks the strong dynamic coupling and interactions among multiple IBRs across the power network, which may adversely affect power system stability.

This paper focuses on the grid-level coordinated optimization of control parameters for both GFM and GFL IBRs to enhance overall system transient dynamic performance under large disturbances. Due to the complex nonlinear dynamics of power systems, transient stability analysis is primarily conducted using time-domain simulations in current industry practice. Mature power system simulation tools, such as PSSE [18], PSCAD [19], and PowerWorld [20], along with continuously advancing simulation technologies such as digital twins [21] and faster-than-real-time simulation [22], [23], enable fast and scalable simulations for accurate stability assessment. Moreover, high-fidelity simulators are widely developed and utilized in the power industry for grid planning and operation, e.g., those embedded in energy management systems, which are readily available for use.

Motivated by these capabilities, this paper proposes a novel framework that integrates a *power system simulator* with *zeroth-order optimization (ZO) algorithms* [24], [25] to optimize IBR control parameters in a model-free manner, thus eliminating the need for explicit mathematical models of complex nonlinear power system dynamics. As illustrated in Figure 1, given a decision \mathbf{x} of IBR control parameters and under disturbances \mathbf{d} , the power system simulator acts as a black-box oracle that can accurately evaluate transient dynamic outcome $f(\mathbf{x}; \mathbf{d})$, such as frequency nadir/zenith, the rate of change of frequency (RoCoF), and the maximum phase angle [26], [27]. ZO algorithms [24], [25], also known as gradient-free methods, offer an effective approach for solving black-box optimization problems using only zeroth-

H. Xu and X. Chen are with the Department of Electrical and Computer Engineering, Texas A&M University, USA. haowen_xu@tamu.edu, xin_chen@tamu.edu. (Corresponding author: Xin Chen).

This work is supported by NSF AMPS Award No. 2523934.

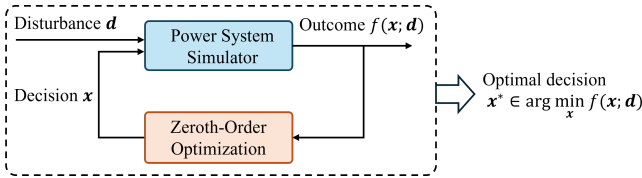


Fig. 1. The simulation-based model-free grid optimization framework.

order information, i.e., function evaluations or simulation outputs. Essentially, ZO methods mimic gradient-descent-type algorithms but replace the true gradient with a zero-order gradient estimator constructed from perturbed function evaluations; see Section III-B for a detailed introduction. As a result, ZO methods provide strong theoretical convergence guarantees [25], [28] and have been used in a broad range of applications, including reinforcement learning [29], neural network training [30], power system control [31], etc.

Contributions. This paper introduces a simulation-based, model-free coordinated optimization framework for tuning IBR control parameters to optimize grid *transient* dynamic performance, such as minimizing frequency fluctuations and improving frequency nadir/zenith. In particular, we propose a *projected multi-point ZO algorithm with adaptive moment estimation (PMZO-Adam)* for effective model-free optimization. Specifically, the proposed algorithm employs projection operations to ensure that the control parameters remain within feasible intervals. Multiple simulations are performed in each iteration to obtain more accurate gradient estimates with reduced variance, and these simulations can be executed in parallel to improve computational efficiency. In addition, the adaptive moment estimation (Adam) method is used to update the descent direction and stepsize simultaneously to accelerate convergence [32]. The key features and advantages of the proposed framework are summarized below:

- 1) *Holistic.* Unlike most existing studies that rely on simplified or linearized models and focus on small-signal stability, the proposed framework leverages high-fidelity simulators to directly optimize grid *transient* dynamic performance. It also captures the complex interdependencies among multiple IBR controllers across the power networks, enabling system-wide optimization rather than isolated tuning of individual facilities.
- 2) *Model-free.* Based on the PMZO-Adam algorithm, the proposed approach requires only simulation outputs for optimization, eliminating the need for explicit mathematical models of complex nonlinear system dynamics.
- 3) *Flexible.* The proposed framework is highly flexible for dynamics-integrated grid optimization problems: (i) it is applicable to various grid configurations, disturbances, and simulation settings by appropriately configuring the simulator; (ii) the optimization objective can be defined as any simulation output; and (iii) it is readily extensible to many other applications by defining the decision variables, such as optimal planning and allocation of GFM/GFL IBRs and stability-integrated power dispatch.

Moreover, a high-fidelity electromagnetic transient (EMT)

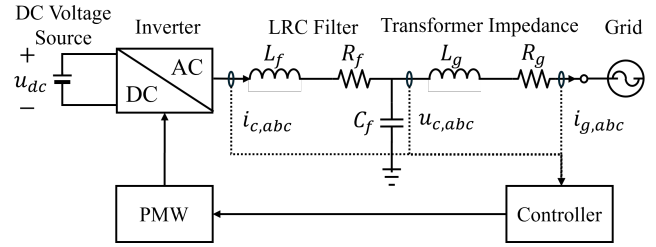


Fig. 2. Typical configuration of a three-phase inverter connected to the power grid (the inverter is connected to the grid through a LRC filter with inductance L_f , resistance, R_f , and capacitance C_f and a transformer modeled with inductance L_g and resistance R_g).

model of a modified IEEE 39-bus system with ten IBRs is developed in Matlab Simulink as the simulation platform, and extensive simulation tests are conducted to demonstrate the effectiveness and optimality of the proposed approach.

Additionally, the proposed framework is intended for offline application, where key IBR control parameters are optimized using simulations and subsequently deployed in real-world systems. This setting leverages the practical availability of accurate power system simulators and is consistent with the industry practice, in which facility control parameters are typically predetermined and adjusted infrequently.

The remainder of this paper is organized as follows: Section II introduces the control architectures and parameters of GFL and GFM inverters. Section III develops the model-free optimization framework based on ZO algorithms. Section IV presents experimental validation and performance analysis, and Section V concludes the paper.

II. CONTROL ARCHITECTURES AND PARAMETERS OF GFL AND GFM INVERTERS

This section presents the typical control architectures of GFM and GFL inverters and identifies the key control parameters that can be tuned to enhance grid dynamic performance. Figure 2 illustrates a typical configuration of a three-phase inverter system connected to the grid. The controller block processes measured signals, such as the three-phase inverter output current $i_{c,abc}$, capacitor voltage $u_{c,abc}$, and grid-side current $i_{g,abc}$, and generates pulse-width modulation (PWM) switching signals for the power electronic switches. The GFL and GFM control strategies are further introduced below.

A. Grid-Following (GFL) Inverter Control

GFL inverters are a widely deployed class of inverters that measure grid states to regulate their output current $i_{c,abc}$ and synchronize with the grid voltage phase angle and frequency [33]. As shown in Figure 3, the three key control components of a GFL inverter include the phase-locked loop (PLL), the frequency-power droop loop, and the current control loop.

The PLL of GFL control is used to estimate the voltage phase angle and grid frequency [10]. Specifically, the PLL employs a proportional-integral (PI) controller to eliminate the frequency estimation error $\Delta\omega$ by driving the q-axis component of the interconnection point voltage, $u_{c,q}$, to zero. The estimated frequency is obtained by adding $\Delta\omega$ to the

nominal grid frequency ω_0 , and integrating this frequency yields the estimated phase angle θ . Thus, the PLL control dynamic equations are formulated as (1):

$$\begin{cases} \dot{\phi}_{\text{PLL}} = K_{i,\text{PLL}} \cdot (u_{c,q} - 0) \\ \Delta\omega = K_{p,\text{PLL}} \cdot (u_{c,q} - 0) + \phi_{\text{PLL}} \\ \dot{\theta} = \Delta\omega + \omega_0 \end{cases} \quad (1)$$

where $K_{i,\text{PLL}}$ and $K_{p,\text{PLL}}$ are the integral and proportional PI parameters of PLL. ϕ_{PLL} is the PLL integrator state variable.

Frequency-power droop control is commonly incorporated into GFL inverter control to regulate active power output in response to variations in grid frequency [34]. Based on the difference between a reference frequency ω_{ref} and the PLL's estimated frequency ω , this droop control generates the active power setpoint P_{set} according to (2), which is then used to determine current reference values ($i_{\text{ref},d}, i_{\text{ref},q}$).

$$P_{\text{set}} = D_{\text{GFL}} \cdot (\omega_{\text{ref}} - \omega) + P_{\text{ref}}. \quad (2)$$

Here, D_{GFL} denotes the droop damping coefficient that influences the frequency response and power-sharing characteristics, and P_{ref} is the predefined active power reference.

In addition, the current control loop generates three-phase PWM control signals ($u_{cs,a}, u_{cs,b}, u_{cs,c}$) to modulate inverter switching and produce the output current $i_{c,abc}$. This loop includes two PI controllers with tunable control parameters, $K_{p,i,\text{GFL}}$ and $K_{i,i,\text{GFL}}$, which significantly influence the transient response of the GFL inverter.

Key GFL Control Parameters. As a result, the dynamic behavior of GFL inverters is governed primarily by the control loops described above and is highly sensitive to the tuning of several key parameters, including the PLL gains $K_{p,\text{PLL}}, K_{i,\text{PLL}}$, the droop control coefficient D_{GFL} , and the current control gains $K_{p,i,\text{GFL}}, K_{i,i,\text{GFL}}$. Coordinated optimization of these parameters is essential to ensure stable operation under varying grid conditions.

B. Grid-Forming (GFM) Inverter Control

In contrast to GFL control, GFM control has the capability to form and regulate the inverter's frequency and voltage [36]. Typical GFM control strategies include droop-based control, virtual synchronous generator (VSG) control, and virtual oscillator control (VOC) [37], etc. In this paper, we adopt the VSG control as a representative example for GFM control, and its architecture is illustrated in Figure 4. This scheme consists of three main components: the VSG control loop, the voltage control loop, and the current control loop.

The VSG control loop consists of two core components: a power-frequency controller and an excitation controller. The power-frequency control dynamics is given by (3) [37]:

$$M_{\text{GFM}} \cdot \dot{\omega} = (P_{\text{ref}} - P_{\text{meas}}) / \omega - D_{\text{GFM}} \cdot (\omega - \omega_{\text{ref}}) \quad (3)$$

where M_{GFM} denotes the emulated inertia parameter, D_{GFM} is the damping coefficient, ω_{ref} is the frequency reference, ω is the frequency established by the GFM inverter, P_{ref} is the active power reference, and P_{meas} is the measured active power, which is typically filtered. Equation (3) emulates the swing dynamics of a synchronous generator, thus enabling

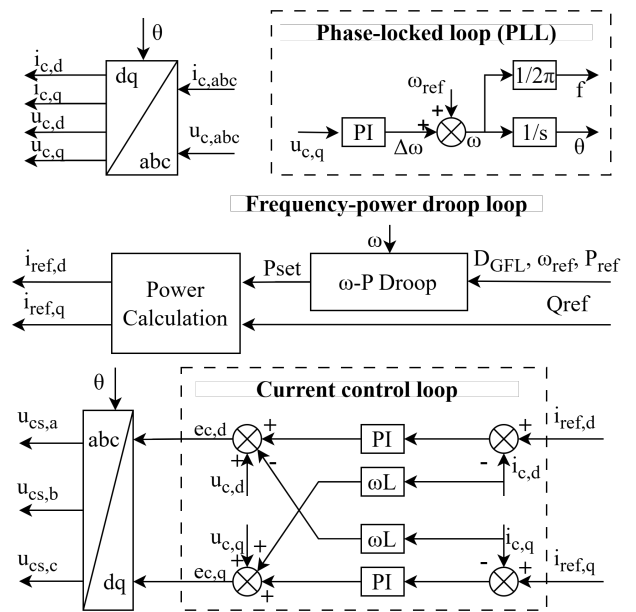


Fig. 3. The phase-locked loop, frequency-power droop control, and current control loop in a GFL inverter (refer to [35] for more details).

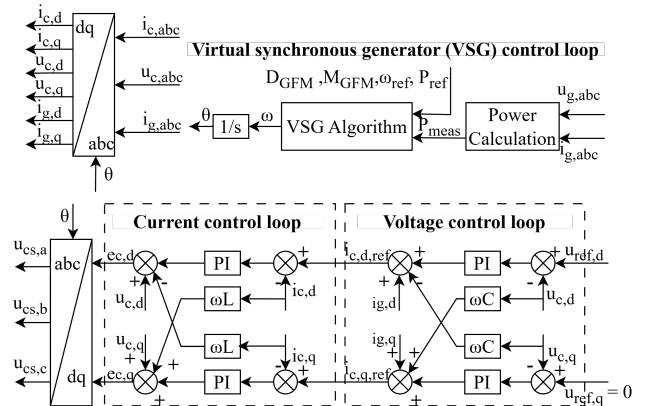


Fig. 4. The virtual synchronous generator (VSG) control loop, voltage control loop, and current control loop in a GFM inverter (refer to [10] for more details).

the GFM inverter to provide synthetic inertia and damping support to the grid.

As illustrated in Figure 4, the voltage control loop regulates the inverter output voltage $u_{c,abc}$ to track the voltage reference ($u_{\text{ref},d}, u_{\text{ref},q} = 0$) and generates current references ($i_{c,d,\text{ref}}, i_{c,q,\text{ref}}$) for the current control loop. These current references are then converted into PWM signals, following a structure similar to that of GFL inverters.

Key GFM Control Parameters. In summary, the performance of a GFM inverter to provide inertia and damping support depends on the coordinated interaction of these control loops described above. Particularly, the dynamic response of the inverter system is highly sensitive to several key parameters, including the inertia parameter M_{GFM} , the damping coefficient D_{GFM} , and the voltage/current loop gains

($K_{p,v,\text{GFM}}, K_{i,v,\text{GFM}}, K_{p,i,\text{GFM}}, K_{i,i,\text{GFM}}$). Appropriate tuning of these parameters is therefore critical for maintaining stable operation and achieving the desired dynamic performance, which is addressed in the following section.

III. PROBLEM FORMULATION AND ALGORITHM DESIGN

In this section, we first formulate the coordinated optimization problem for IBR control parameters to enhance transient grid dynamic performance. We then introduce the preliminaries of ZO and the Adam method. Lastly, we propose the PMZO-Adam algorithm for simulation-based model-free optimization to solve the formulated problem.

A. Problem Formulation

Consider a generic problem formulation (4) for grid-level coordinated optimization of IBR control parameters:

$$\min_{\mathbf{x} \in \mathcal{X}} f(\mathbf{x}) := \sum_{s \in \mathcal{S}} \alpha_s \cdot \hat{f}(\mathbf{x}; \mathbf{d}_s), \quad (4)$$

where the decision variable \mathbf{x} denotes the key control parameters of all IBRs in the grid, and \mathcal{X} is the feasible set, such as the physical upper and lower limits of \mathbf{x} . s denotes a disturbance scenario in the scenario set \mathcal{S} , and \mathbf{d}_s represents a specific disturbance, e.g., load change and line contingency. α_s is the weight factor of scenario s , and \hat{f} represents the grid transient dynamic performance metrics to be optimized, such as the frequency nadir or zenith, RoCoF, frequency fluctuations, maximum phase angle, etc. Hence, problem (4) aims to optimize the overall grid dynamic performance, weighted across a predefined set of disturbance scenarios.

Specific grid transient dynamic performance metrics \hat{f} can be flexibly adapted based on practical considerations. For instance, we aim to mitigate frequency nadir or zenith and suppress frequency oscillations after a disturbance. Accordingly, \hat{f} can be formulated as (5), where the scenario index s is omitted for notational simplicity.

$$\hat{f} := \sum_{i \in \mathcal{N}_{\text{opt}}} \left[\lambda \cdot \max_{t \in \mathcal{T}_{\text{dev}}} |\omega_{i,t} - \omega_0| + (1 - \lambda) \cdot \frac{1}{|\mathcal{T}_{\text{osc}}|} \sum_{t \in \mathcal{T}_{\text{osc}}} (\omega_{i,t} - \bar{\omega}_{i,\mathcal{T}_{\text{osc}}})^2 \right]. \quad (5)$$

Here, i denotes the bus index, and \mathcal{N}_{opt} is the set of buses whose frequencies are considered in the optimization. t denotes the time index. $\mathcal{T}_{\text{dev}} := \{t_d, t_d + \Delta t, \dots, T\}$ denotes the discrete time window over which the maximum frequency deviation is evaluated, where t_d is the disturbance occurrence time, Δt is the time step size, and T is the final time step. $\omega_{i,t}$ is the frequency of bus i at time t , and ω_0 is the nominal frequency (e.g., 60 Hz in the U.S.). $\mathcal{T}_{\text{osc}} := \{t_o, t_o + \Delta t, \dots, T\}$ denotes the discrete time window over which the post-disturbance frequency oscillation is evaluated, where t_o is the corresponding initial time step. $\bar{\omega}_{i,\mathcal{T}_{\text{osc}}}$ denotes the average value of the frequency $\omega_{i,t}$ over the time window \mathcal{T}_{osc} .

Hence, the grid dynamic performance metric \hat{f} defined in (5) is a weighted multi-objective function that balances the maximum frequency deviation (first term) and the empirical

variance of the frequency (second term), which captures post-disturbance oscillations, with the weight factor $\lambda \in [0, 1]$.

The decision variable vector \mathbf{x} consists of the key control parameters of IBRs. As introduced in Section II, \mathbf{x} includes $\{K_{p,\text{PLL}}, K_{i,\text{PLL}}, D_{\text{GFL}}, K_{p,i,\text{GFL}}, K_{i,i,\text{GFL}}\}$ for a GFL inverter, and $\{M_{\text{GFM}}, D_{\text{GFM}}, K_{p,v,\text{GFM}}, K_{i,v,\text{GFM}}, K_{p,i,\text{GFM}}, K_{i,i,\text{GFM}}\}$ for a GFM inverter. Each entry x_j in \mathbf{x} is subject to the feasible interval $[\underline{x}_j, \bar{x}_j]$, and thus the feasible set is $\mathcal{X} := \prod_j [\underline{x}_j, \bar{x}_j]$.

Remark. A critical challenge in solving (4) is the absence of an explicit mathematical model of the grid transient dynamic performance function $\hat{f}(\mathbf{x}; \mathbf{d}_s)$. This function represents the input-output mapping governed by the complex nonlinear power system dynamics and is generally intractable to derive. To address this challenge, we propose integrating a high-fidelity power system simulator with ZO algorithms to solve (4) in a model-free manner. In this framework, the simulator acts as a black-box oracle that outputs the value of $\hat{f}(\mathbf{x}; \mathbf{d}_s)$ for a given decision \mathbf{x} and disturbance \mathbf{d}_s . As our framework enables simulation-based model-free optimization, it can flexibly accommodate any transient dynamic performance metrics \hat{f} constructed from simulation outputs.

B. Zeroth-Order Optimization and Adam Method

This subsection presents the preliminaries of ZO algorithms and the Adam method, which incorporates adaptive moment estimation to accelerate convergence.

1) *Zeroth-Order Optimization (ZO):* ZO methods have been widely applied to solve black-box optimization and control problems. In essence, ZO methods mimic gradient-based algorithms but replace the unavailable gradient with a zeroth-order gradient estimator constructed from perturbed function evaluations. Depending on the number of queried function evaluations at each iteration, ZO methods can be categorized into three classes: single-point, two-point, and multi-point schemes [24], [38], [39].

Consider solving the unconstrained version of (4) without the feasible set \mathcal{X} . The two-point ZO method is given by:

$$\mathbf{x}_{k+1} = \mathbf{x}_k - \eta \cdot G_f^{(2)}(\mathbf{x}_k; r, \mathbf{u}_k), \quad k = 0, 1, \dots, \quad (6)$$

where η denotes the step size, and $G_f^{(2)}(\mathbf{x}; r, \mathbf{u})$ is the two-point ZO gradient estimator defined as (7):

$$G_f^{(2)}(\mathbf{x}; r, \mathbf{u}) := \frac{d}{2r} \left(f(\mathbf{x} + r\mathbf{u}) - f(\mathbf{x} - r\mathbf{u}) \right) \mathbf{u}. \quad (7)$$

Here, d denotes the dimension of \mathbf{x} , $r > 0$ is a scalar parameter called the smoothing radius, and $\mathbf{u} \in \mathbb{R}^d$ is a random direction vector independently sampled at each iteration k from the uniform distribution on the unit sphere \mathbb{S}_{d-1} . Two function evaluations at the points $\mathbf{x} + r\mathbf{u}$ and $\mathbf{x} - r\mathbf{u}$ are used to construct $G_f^{(2)}(\mathbf{x}; r, \mathbf{u})$, which serves as a biased estimator of the true gradient $\nabla f(\mathbf{x})$; see [25] for more details.

2) *The Adam Method:* The adaptive moment estimation (Adam) [32] method is one of the most widely used first-order gradient-based optimization methods in machine learning. It leverages past gradients to update both descent directions and step sizes, which effectively accelerates convergence. Reference [40] extends this idea to the black-box

optimization settings, where explicit gradients are unavailable. Specifically, the Adam update at each iteration k is given by (8):

$$\mathbf{m}_k = \beta_1 \mathbf{m}_{k-1} + (1 - \beta_1) \mathbf{g}_k, \quad \mathbf{v}_k = \beta_2 \mathbf{v}_{k-1} + (1 - \beta_2) \mathbf{g}_k^2, \quad (8a)$$

$$\hat{\mathbf{m}}_k = \mathbf{m}_k / (1 - \beta_1^k), \quad \hat{\mathbf{v}}_k = \mathbf{v}_k / (1 - \beta_2^k), \quad (8b)$$

$$\mathbf{x}_{k+1} = \mathbf{x}_k - \eta \frac{\hat{\mathbf{m}}_k}{\sqrt{\hat{\mathbf{v}}_k + \varepsilon}}. \quad (8c)$$

In (8a), \mathbf{g}_k denotes the gradient estimate at iteration k . \mathbf{m}_k and \mathbf{v}_k represent the first and second moment estimates, respectively. Equation (8a) updates the exponential moving averages of the gradient (\mathbf{m}_k) and the squared gradient (\mathbf{v}_k), where the hyper-parameters $\beta_1, \beta_2 \in [0, 1)$ control the exponential decay rates of these moving averages. Equation (8b) computes the bias-corrected first and second moment estimates, where β_1^k and β_2^k denote β_1 and β_2 to the power of k , respectively. In (8c), ε is a very small positive constant introduced to prevent division by zero. See [32] for more details on the algorithm.

C. Our Algorithm for Coordinated IBR Control Optimization

Built upon the methods described above, we propose the PMZO-Adam algorithm (i.e., Algorithm 1) to effectively solve the coordinated IBR control parameter optimization problem (4). To further reduce the variance in gradient estimation and improve convergence, we adopt a multi-point ZO method that performs N batches of two-point evaluations and uses their average as the gradient estimate.

Specifically, at each iteration k , Algorithm 1 samples N random perturbation directions $\{\mathbf{u}_{k,n}\}_{n=1}^N$ from the uniform distribution on the unit sphere \mathbb{S}_{d-1} (Step 6). Then, high-fidelity power system simulations are executed in parallel to evaluate the grid transient dynamic performance \hat{f} for the perturbed decisions $\mathbf{x}_k + r_k \mathbf{u}_{k,n}$ and $\mathbf{x}_k - r_k \mathbf{u}_{k,n}$ under each disturbance \mathbf{d}_s for $s \in \mathcal{S}$. This yields the objective function evaluations $f(\mathbf{x}_k + r_k \mathbf{u}_{k,n})$ and $f(\mathbf{x}_k - r_k \mathbf{u}_{k,n})$ in (4) for $n = 1, \dots, N$ (Step 7). Next, these function evaluations are used to construct the multi-point ZO gradient estimate \mathbf{g}_k as defined in (9), which averages the two-point gradient estimates (7) over N batches to reduce estimation variance. In Step 12, the Adam method (8) is employed to update the iterate. Moreover, the projection operator, $\text{Proj}_{\mathcal{X}}(\mathbf{y}) := \arg \min_{\mathbf{x} \in \mathcal{X}} \|\mathbf{x} - \mathbf{y}\|_2^2$, is incorporated into (10) to ensure that all iterates remain within the feasible set \mathcal{X} . In addition, the stepsize η_k and smoothing radius r_k decay monotonically according to (11) in Step 13 to enhance convergence, enabling robust exploration in the early iterations while allowing precise fine-tuning near convergence.

Remark. In Algorithm 1, each iteration requires $2N \cdot |\mathcal{S}|$ simulations to construct the multi-point gradient estimate \mathbf{g}_k . Nevertheless, these simulations are mutually independent and can therefore be executed fully in parallel, so the clock time is essentially equivalent to that of a single simulation. Additionally, advanced simulation techniques, such as hybrid phasor-EMT simulations [41], significantly improve computational efficiency, thereby enhancing the scalability of the proposed algorithm for large-scale power grids.

Algorithm 1 Projected Multi-Point ZO-Adam (PMZO-Adam) for Coordinated IBR Control Optimization.

- 1: **Input:** Disturbance scenario set \mathcal{S} , batch size N , max iteration number K , tolerance τ , Adam parameters $\beta_1, \beta_2 \in [0, 1)$, $\varepsilon > 0$, decay rates $\gamma_\eta, \gamma_r \in (0, 1)$, and minimum bounds η_{\min}, r_{\min} .
 - 2: **Initialize:** IBR control parameters $\mathbf{x}_1 \in \mathcal{X}$, moments $\mathbf{m}_0 = \mathbf{0}$, $\mathbf{v}_0 = \mathbf{0}$, step size η_1 , smoothing radius r_1 .
 - 3: **for** $k = 1, 2, \dots, K$ **do**
 - 4: **(1) Perform Parallel Simulations:**
 - 5: **for** $n = 1, \dots, N$ in parallel **do**
 - 6: Sample random direction $\mathbf{u}_{k,n} \sim \text{Unif}(\mathbb{S}_{d-1})$.
 - 7: Execute simulations for each disturbance \mathbf{d}_s for $s \in \mathcal{S}$ in parallel to obtain the objective function values $f(\mathbf{x}_k + r_k \mathbf{u}_{k,n})$ and $f(\mathbf{x}_k - r_k \mathbf{u}_{k,n})$.
 - 8: **end for**
 - 9: **(2) Gradient Estimation:**
 - 10: Compute average multi-point ZO gradient estimate:

$$\mathbf{g}_k = \frac{1}{N} \sum_{n=1}^N \left[\frac{d}{2r_k} (f(\mathbf{x}_k + r_k \mathbf{u}_{k,n}) - f(\mathbf{x}_k - r_k \mathbf{u}_{k,n})) \mathbf{u}_{k,n} \right]. \quad (9)$$
 - 11: **(3) Optimization Update:**
 - 12: Compute the moment estimates $\mathbf{m}_k, \mathbf{v}_k, \hat{\mathbf{m}}_k, \hat{\mathbf{v}}_k$ according to (8a) and (8b), and update the iterate by:

$$\mathbf{x}_{k+1} = \text{Proj}_{\mathcal{X}} \left(\mathbf{x}_k - \eta_k \frac{\hat{\mathbf{m}}_k}{\sqrt{\hat{\mathbf{v}}_k + \varepsilon}} \right). \quad (10)$$
 - 13: Update the stepsize and smoothing radius by:

$$\eta_{k+1} = \max(\gamma_\eta \cdot \eta_k, \eta_{\min}), r_{k+1} = \max(\gamma_r \cdot r_k, r_{\min}). \quad (11)$$
 - 14: **(4) Convergence Check:**
 - 15: If $\|\mathbf{x}_{k+1} - \mathbf{x}_k\| \leq \tau$, terminate.
 - 16: **end for**
 - 17: **Output:** Optimized IBR control parameters $\mathbf{x}^* = \mathbf{x}_{k+1}$.
-

IV. SIMULATION TESTS AND ANALYSIS

This section evaluates the performance of the proposed PMZO-Adam algorithm using high-fidelity EMT simulations under two typical disturbance scenarios, namely sudden load change and line contingency. Then, the impacts of the batch size N and the Adam method are studied.

A. Simulation Setup

A high-fidelity EMT dynamic model for a modified IEEE 39-bus system is developed in MATLAB Simulink and used as the test system. As shown in Figure 5, the system includes six GFL and four GFM IBRs, each equipped with realistic control loops as described in Section II. The detailed system parameters, initial control settings, the feasible set \mathcal{X} , and the hyperparameters of the PMZO-Adam algorithm are provided in the Appendix. Below, we consider two representative disturbance scenarios, i.e., sudden load change and line contingency, and optimize the IBR control parameters separately

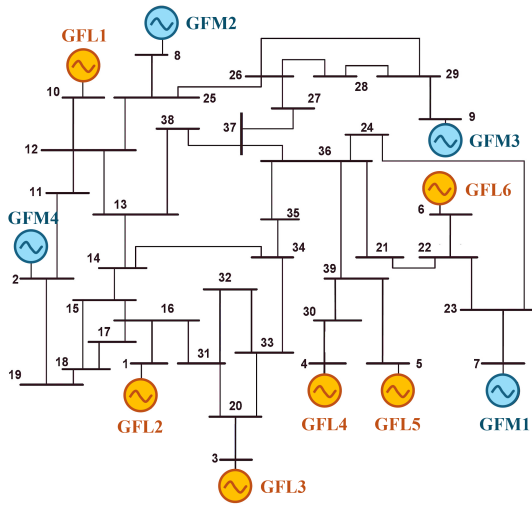


Fig. 5. The modified IEEE 39-bus power system for simulation tests.

for each scenario to enhance the grid transient frequency performance as defined in (5). The buses connected to IBRs are selected as the set \mathcal{N}_{opt} in (5), whose transient frequency behaviors are considered for optimization. Since only primary frequency control is implemented, the system can stabilize the grid frequency after disturbances while not restoring the nominal frequency value.

The simulations are implemented in MATLAB R2025a on a computing platform equipped with an AMD Ryzen 5 8400F CPU, an NVIDIA GeForce RTX 5060 GPU, and 48 GB of RAM. The EMT Simulink model is executed with a time step of $50\mu\text{s}$. Each simulation spans 5 seconds and takes approximately 40 seconds on average to complete.

B. Scenario 1: Sudden Load Change

In this subsection, we consider a large load increase disturbance that causes a significant drop in grid frequency. Specifically, an additional 1 GW load is suddenly applied at bus 26 at time $t=1\text{s}$, while the total load in the system is 6 GW. The proposed algorithm is then employed to optimize the IBR control parameters. The optimization results are presented in Figures 6, 7, and 8, as well as in Table IV.

Figure 6 illustrates the convergence of the objective function value, which decreases from 0.1751 to 0.0421, indicating a 76.0% improvement in grid frequency transient performance after optimizing the IBR control parameters. Moreover, a rapid decrease in the objective value is observed within the first 10 iterations, demonstrating the fast convergence of the proposed algorithm. The small fluctuations in subsequent iterations arise from the random perturbations for gradient estimation in the algorithm. Figure 7 shows the corresponding convergence of the key IBR control parameters, i.e., the decision variables \mathbf{x} .

The grid transient frequency responses under the Scenario-1 disturbance, before and after optimization, are compared and illustrated in Figure 8. We present the frequency dynamics of the buses connected to GFL1, GFL4, GFM3, and GFM4,

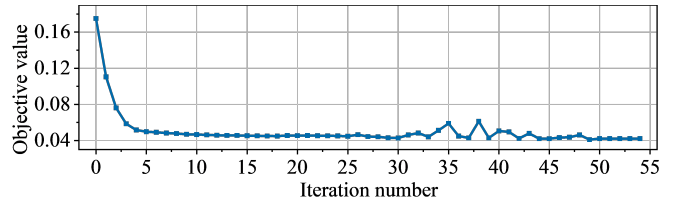


Fig. 6. The convergence of objective function value in Scenario 1.

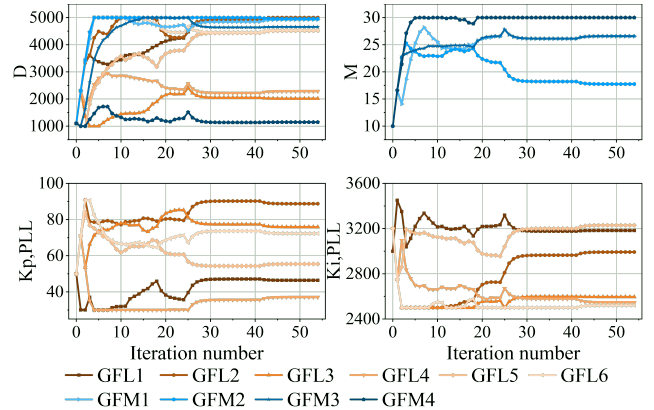


Fig. 7. The convergence of key IBR control parameters in Scenario 1.

and GFM4, as they are most affected by the disturbance. It is observed that both the frequency nadirs and fluctuations are significantly improved when using the optimized IBR control parameters generated by the proposed algorithm. For example, GFM3 is located close to the load disturbance at bus 26 and exhibits a substantial frequency response; after optimization, both its damping and inertia parameters are increased to provide stronger local support and mitigate overall grid frequency deviations. These results demonstrate that the proposed algorithm effectively optimizes the IBR control parameters in response to load disturbances, leading to significant improvements in grid transient performance.

C. Scenario 2: Line Contingency

In this subsection, we consider a severe line contingency disturbance in which the transmission line between bus 18

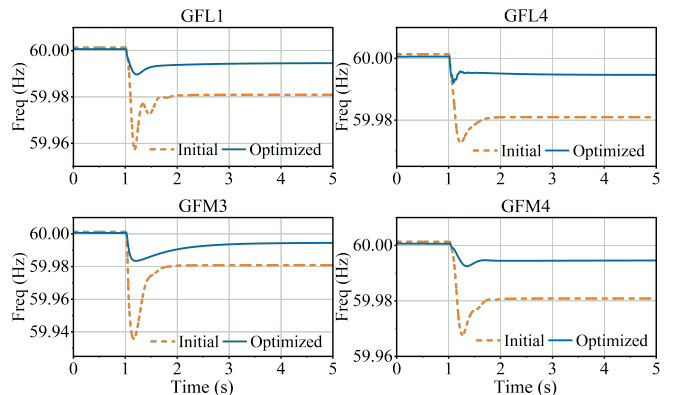


Fig. 8. Frequency responses of four IBR buses under Scenario-1 disturbance, using the IBR control parameters before and after optimization.

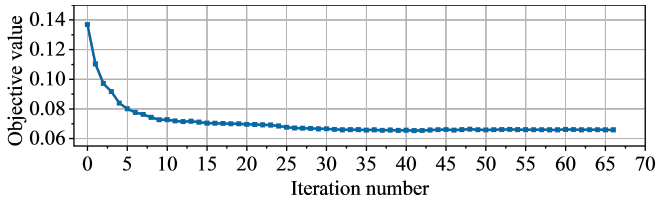


Fig. 9. The convergence of objective function value in Scenario 2.

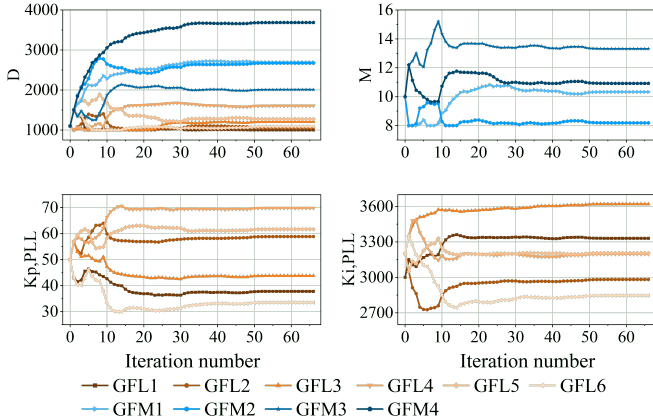


Fig. 10. The convergence of key IBR control parameters in Scenario 2.

and bus 19 is suddenly opened at $t=1$ s, which alters the network topology and causes large frequency deviations. The results are presented in Figures 9, 10, 11, and Table V.

Figure 9 illustrates the convergence of the objective function value, which is reduced from 0.1369 to 0.066, corresponding to a 51.8% improvement. A similarly rapid decrease is observed within the first 10 iterations. Figure 10 shows the convergence of the key IBR control parameters during the optimization process. Figure 11 compares the frequency responses of the four most affected IBR buses before and after optimization. The results show that both the maximum frequency deviations and frequency oscillations are significantly mitigated when the optimized control parameters obtained by the proposed algorithm are adopted. For instance, GFM4, which is closest to the fault, has its damping parameter D substantially increased to improve transient frequency behavior, while $K_{p,PLL}$ of GFL1 is reduced to prevent excessive overshoot. This highlights the necessity of coordinated parameter tuning across different IBRs in the grid for effective disturbance mitigation.

The case studies above demonstrate the robustness and effectiveness of the proposed method in handling different types of disturbances. The method can also be used to identify optimal IBR control parameters that balance transient dynamic performance across multiple disturbance scenarios.

D. Impact of Batch Size N

In the PMZO-Adam algorithm (Algorithm 1), a multi-point zeroth-order gradient estimator with N batches is employed to reduce variance and enhance convergence. In the previous tests above, the batch size N was set to 2. In

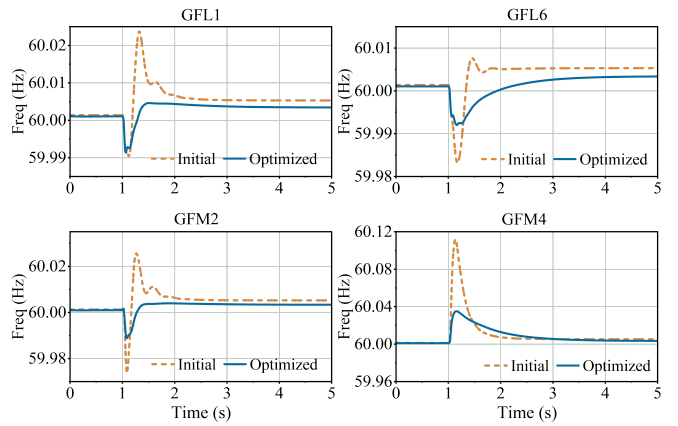


Fig. 11. Frequency responses of four IBR buses under Scenario-2 disturbance, using the IBR control parameters before and after optimization.

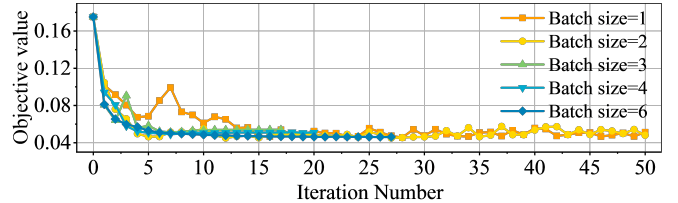


Fig. 12. The convergence of objective value under different batch sizes.

this subsection, we examine the impact of the batch size N on the algorithm using Scenario 1 as the test case.

Figure 12 illustrates the convergence of the objective function value for different batch sizes N . Small batch sizes ($N=1,2$) exhibit significant fluctuations due to the high variance of the gradient estimates, with $N=1$ showing a prolonged exploration phase before stabilization. As N increases, the convergence curves become smoother and faster. In particular, a batch size of $N=6$ yields the most favorable convergence trajectory with the steepest descent and the lowest final objective value. This observation is consistent with the intuition that a larger batch size N generally reduces the gradient estimation variance and leads to more stable convergence. Although a larger N requires more simulation evaluations, these evaluations can be executed fully in parallel within the proposed framework. Nevertheless, in highly nonconvex optimization landscapes, the large variance associated with small batch sizes can facilitate broader exploration and occasionally help the algorithm escape local minima [42]. Hence, selecting the right batch size is important to balance convergence rate, stability, and exploration capability, which will be studied in future work.

E. Effect of the Adam Method

As discussed in Section III-B, the Adam method improves convergence through adaptive moment mechanisms. This subsection examines the effect of incorporating Adam into the proposed algorithm. The tests are conducted under Scenario 1 disturbance with a batch size of $N=2$ and an initial stepsize of $\eta_1=0.1$. Figure 13 presents the ablation study on the Adam method. The proposed PMZO-Adam algorithm

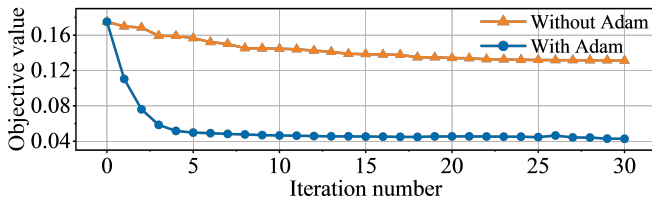


Fig. 13. The convergence of objective value with and without Adam.

exhibits significantly faster convergence and achieves a lower final objective value than the variant without Adam. This result demonstrates the effectiveness of incorporating Adam to accelerate convergence, which adaptively updates the stepsize and descent direction based on gradient history.

V. CONCLUSION

This paper introduces a simulation-based, model-free framework for the coordinated optimization of IBR control parameters to enhance grid-level transient dynamic performance. The proposed PMZO-Adam algorithm solves the optimization problem in a model-free manner, eliminating the need for explicit mathematical models of complex nonlinear power system dynamics. Extensive EMT simulations on a modified IEEE 39-bus system demonstrate that the proposed approach significantly mitigates maximum frequency deviations and frequency fluctuations under large disturbances. In addition, the incorporation of multi-point ZO and the Adam method effectively reduces gradient estimation variance and accelerates convergence. Future work will focus on providing a theoretical performance analysis of the proposed algorithm and extending the framework to online settings and applications with more realistic constraints.

APPENDIX

This appendix presents the simulation settings for the modified IEEE 39-bus system shown in Figure 5. Table I summarizes the initial power flow data and baseline control parameters for all IBRs. Table II defines the feasible parameter set \mathcal{X} by specifying the physical lower and upper bounds of these control parameters. Table III provides the hyperparameter settings used in the PMZO-Adam optimization algorithm. Tables IV and V report the optimal parameter settings for Scenario 1 and Scenario 2, respectively.

REFERENCES

- [1] Y. Gu and T. C. Green, "Power system stability with a high penetration of inverter-based resources," *Proceedings of the IEEE*, vol. 111, no. 7, pp. 832–853, 2023.
- [2] F. Milano, F. Dörfler, G. Hug, D. J. Hill, and G. Verbič, "Foundations and challenges of low-inertia systems (invited paper)," in *2018 Power Systems Computation Conference (PSCC)*, pp. 1–25, 2018.
- [3] U. Markovic, O. Stanojevic, P. Aristidou, E. Vrettos, D. Callaway, and G. Hug, "Understanding small-signal stability of low-inertia systems," *IEEE Transactions on Power Systems*, vol. 36, no. 5, pp. 3997–4017, 2021.
- [4] A. Arzani, P. Arunagirinathan, and G. K. Venayagamoorthy, "Stochastic subspace identification validation of PV inverter operation improvement with optimally-tuned controllers," in *2018 Clemson University Power Systems Conference (PSC)*, pp. 1–6, 2018.

- [5] I. Dagal, B. Erol, A. Harrison, W. F. Mbasso, and A. Ibrahim, "Enhancing dynamic control and stability assessment of cessna 172 aircraft with a PID controller for new pilot trainees," *International Journal of Aeronautical and Space Sciences*, vol. 26, pp. 2087 – 2104, 2025.
- [6] M. Chen, D. Zhou, A. Tayyebi, E. Prieto-Araujo, F. Dörfler, and F. Blaabjerg, "On power control of grid-forming converters: Modeling, controllability, and full-state feedback design," *IEEE Transactions on Sustainable Energy*, vol. 15, pp. 68–80, 2022.
- [7] W. Zhang, Y. Cui, and X. Ding, "An improved analytical tuning rule of a robust PID controller for integrating systems with time delay based on the multiple dominant pole-placement method," *Symmetry*, vol. 12, p. 1449, 2020.
- [8] F. Arraño-Vargas, Z. Shen, S. Jiang, J. Fletcher, and G. Konstantinou, "Challenges and mitigation measures in power systems with high share of renewables—the australian experience," *Energies*, 2022.
- [9] M. Khan, W. Wu, and L. Li, "Grid-forming control for inverter-based resources in power systems: A review on its operation, system stability, and prospective," *IET Renewable Power Generation*, 2024.
- [10] E. A. S. Ducoin, Y. Gu, B. Chaudhuri, and T. C. Green, "Analytical design of contributions of grid-forming and grid-following inverters to frequency stability," *IEEE Transactions on Power Systems*, vol. 39, pp. 6345–6358, 2024.
- [11] H. Ma, F. Min, G. Huang, and Y. Dou, "Chaos and bifurcation behavior in a fundamental power system with electromagnetic disturbance and load disturbance," *AIP Advances*, 2019.
- [12] J. Vlachogiannis and S. M. I. N. D. Hatzigiorgiou, "Reinforcement learning for reactive power control," *IEEE Transactions on Power Systems*, vol. 19, pp. 1317–1325, 2004.
- [13] Z. Huang, T. Yu, Z. Pan, B. Deng, X. Zhang, Y. Wu, and Q. Ding, "Stochastic dynamic power dispatch with high generalization and few-shot adaption via contextual meta graph reinforcement learning," *International Journal of Electrical Power & Energy Systems*, vol. 162, p. 110272, 2024.
- [14] H. Verdejo, V. Pino, W. Kliemann, C. Becker, and J. Delpiano, "Implementation of particle swarm optimization (PSO) algorithm for tuning of power system stabilizers in multimachine electric power systems," *Energies*, 2020.
- [15] F. Bano, M. Ayaz, D. e Zehra Baig, and S. M. H. Rizvi, "Intelligent control algorithms for enhanced frequency stability in single and interconnected power systems," *Electronics*, 2024.
- [16] S. Li, W. Wu, J. Xu, J. Dong, F. Wang, and Q. Yuan, "Zeroth-order feedback optimization for inverter-based volt-var control in wind farm," in *2024 The 9th International Conference on Power and Renewable Energy (ICPRE)*, pp. 1384–1389, IEEE, 2024.
- [17] D. S. Zalkind, E. Dall'Anese, and L. Y. Pao, "Automatic controller tuning using a zeroth-order optimization algorithm," *Wind Energy Science*, vol. 5, no. 4, pp. 1579–1600, 2020.
- [18] Siemens Energy, Inc., *PSSE: Power System Simulator for Engineering*, 2025. Version 36.1.
- [19] Manitoba Hydro International Ltd., *PSCAD: Power Systems Computer Aided Design*, 2025. Version 5.0.2.
- [20] PowerWorld Corporation, *PowerWorld Simulator*, 2025. Version 23.
- [21] H. Pan, Z. Dou, Y. Cai, W. Li, X. Lei, and D. Han, "Digital twin and its application in power system," in *2020 5th International Conference on Power and Renewable Energy (ICPRE)*, pp. 21–26, IEEE, 2020.
- [22] B. Sullivan, J. Shi, M. Mazzola, and B. Saravi, "Faster-than-real-time power system transient stability simulation using parallel general norton with multiport equivalent (PGNME)," in *2017 IEEE Power & Energy Society General Meeting (PESGM)*, pp. 1–5, 2017.
- [23] C. Wang, S. Liang, X. Jia, and S. Jin, "High-performance computing on power system transient stability analysis: A review," in *2023 North American Power Symposium (NAPS)*, pp. 01–06, 2023.
- [24] S. Liu, P.-Y. Chen, B. Kailkhura, G. Zhang, A. O. Hero III, and P. K. Varshney, "A primer on zeroth-order optimization in signal processing and machine learning: Principals, recent advances, and applications," *IEEE Signal Processing Magazine*, vol. 37, no. 5, pp. 43–54, 2020.
- [25] Y. Nesterov and V. Spokoiny, "Random gradient-free minimization of convex functions," *Foundations of Computational Mathematics*, vol. 17, no. 2, pp. 527–566, 2017.
- [26] M. Tuo and X. Li, "Convolutional neural network-based RoCoF-constrained unit commitment," *arXiv preprint arXiv:2309.02650*, 2023.
- [27] D. Gan, R. J. Thomas, and R. D. Zimmerman, "Stability-constrained

TABLE I
INVERTER-BASED RESOURCES PARAMETERS

IBR Name	IBR Information			Initial Control Parameters Settings							
	Bus	P_{init} (MW)	Q_{init} (MVar)	D	M	$K_{i,\text{PLL}}$	$K_{p,\text{PLL}}$	$K_{i,v}$	$K_{p,v}$	$K_{i,i}$	$K_{p,i}$
IBR1-GFL1	10	2	0.1	1100	–	3000	50	–	–	200	50
IBR2-GFL2	1	2	0.1	1100	–	3200	50	–	–	200	50
IBR3-GFL3	3	2	0.1	1100	–	3200	50	–	–	100	20
IBR4-GFL4	4	2	0.1	1100	–	3200	50	–	–	200	50
IBR5-GFL5	5	2	0.1	1100	–	3200	50	–	–	200	70
IBR6-GFL6	6	2	0.1	1100	–	3200	50	–	–	200	50
IBR7-GFM1	2	3	0	1100	10	–	–	40	10	12.5	2.5
IBR8-GFM2	9	3	0	1100	10	–	–	40	10	12.5	2.5
IBR9-GFM3	8	4	0	1100	10	–	–	40	10	12.5	2.5
IBR10-GFM4	7	5	0	1100	10	–	–	40	10	12.5	2.5

TABLE II
FEASIBLE INTERVALS OF KEY IBR CONTROL PARAMETERS

IBR Name	D	M	$K_{i,\text{PLL}}$	$K_{p,\text{PLL}}$	$K_{i,v}$	$K_{p,v}$	$K_{i,i}$	$K_{p,i}$
IBR1-GFL1	[1000, 5000]	–	[2500,4000]	[30,100]	–	–	[20, 300]	[20,70]
IBR2-GFL2	[1000, 5000]	–	[2500,4000]	[30,100]	–	–	[20, 300]	[20,70]
IBR3-GFL3	[1000, 5000]	–	[2500,4000]	[30,100]	–	–	[20, 300]	[20,70]
IBR4-GFL4	[1000, 5000]	–	[2500,4000]	[30,100]	–	–	[20, 300]	[20,70]
IBR5-GFL5	[1000, 5000]	–	[2500,4000]	[30,100]	–	–	[20, 300]	[20,70]
IBR6-GFL6	[1000, 5000]	–	[2500,4000]	[30,100]	–	–	[20, 300]	[20,70]
IBR7-GFM1	[1000, 5000]	[8, 30]	–	–	[20, 60]	[5, 40]	[8, 20]	[1, 5]
IBR8-GFM2	[1000, 5000]	[8, 30]	–	–	[20, 60]	[5, 40]	[8, 20]	[1, 5]
IBR9-GFM3	[1000, 5000]	[8, 30]	–	–	[20, 60]	[5, 40]	[8, 20]	[1, 5]
IBR10-GFM4	[1000, 5000]	[8, 30]	–	–	[20, 60]	[5, 40]	[8, 20]	[1, 5]

TABLE III
HYPERPARAMETERS OF THE PMZO-ADAM ALGORITHM

Parameter	Value	Parameter	Value	Parameter	Value
η_1	0.1	R	70	τ	10^{-4}
δ_1	0.1	N	2	t_d (s)	1
γ_1	0.9	β_1	0.5	T (s)	5
γ_δ	0.95	β_2	0.99	t_o (s)	4.5
η_{min}	0.001	ϵ	10^{-8}	α	0.5
δ_{min}	0.001				

optimal power flow,” *IEEE Transactions on Power Systems*, vol. 15, no. 2, pp. 535–540, 2000.

- [28] X. Chen, J. I. Poveda, and N. Li, “Continuous-time zeroth-order dynamics with projection maps: Model-free feedback optimization with safety guarantees,” *IEEE Transactions on Automatic Control*, vol. 70, no. 8, pp. 5005–5020, 2025.
- [29] Y. Li, Y. Tang, R. Zhang, and N. Li, “Distributed reinforcement learning for decentralized linear quadratic control: A derivative-free policy optimization approach,” *arXiv preprint arXiv:1912.09135*, 2019.
- [30] P.-Y. Chen, H. Zhang, Y. Sharma, J. Yi, and C.-J. Hsieh, “Zoo: Zeroth order optimization based black-box attacks to deep neural networks without training substitute models,” in *Proceedings of the 10th ACM Workshop on Artificial Intelligence and Security*, pp. 15–26, 2017.
- [31] X. Chen, J. I. Poveda, and N. Li, “Safe model-free optimal voltage control via continuous-time zeroth-order methods,” in *2021 60th IEEE Conference on Decision and Control (CDC)*, pp. 4064–4070, IEEE, 2021.
- [32] D. P. Kingma and J. Ba, “Adam: A method for stochastic optimization,” *arXiv preprint arXiv:1412.6980*, 2014.
- [33] W. Du, F. K. Tuffner, K. P. Schneider, R. H. Lasseter, J. Xie, Z. Chen, and B. Bhattacharai, “Modeling of grid-forming and grid-following inverters for dynamic simulation of large-scale distribution systems,” *IEEE Transactions on Power Delivery*, vol. 36, no. 4, pp. 2035–2045, 2020.
- [34] T. Ochoa, B. Chaudhuri, and M. O’Malley, “Optimal control for robust

dynamic performance in inverter-dominated power systems. part I: Modeling and problem formulation,” *Authorea Preprints*, 2025.

- [35] M. Nestor, J. Wang, N. Zhang, and F. Teng, “Data-driven communication and control design for distributed frequency regulation with black-box inverters,” *arXiv preprint arXiv:2510.17769*, 2025.
- [36] D. B. Rathnayake, M. Akrami, C. Phurailatpam, S. P. Me, S. Hadavi, G. Jayasinghe, S. Zabihi, and B. Bahrani, “Grid forming inverter modeling, control, and applications,” *IEEE Access*, vol. 9, pp. 114781–114807, 2021.
- [37] M. Tozak, S. Taskin, I. Sengor, and B. P. Hayes, “Modeling and control of grid forming converters: A systematic review,” *IEEE Access*, vol. 12, pp. 107818–107843, 2024.
- [38] X. Chen, Y. Tang, and N. Li, “Improve single-point zeroth-order optimization using high-pass and low-pass filters,” in *International Conference on Machine Learning*, pp. 3603–3620, PMLR, 2022.
- [39] X. Chen and Z. Ren, “Accelerating single-point zeroth-order optimization with regression-based gradient surrogates,” *arXiv preprint arXiv:2507.04223*, 2026.
- [40] X. Chen, S. Liu, K. Xu, X. Li, X. Lin, M. Hong, and D. Cox, “Zo-adamm: Zeroth-order adaptive momentum method for black-box optimization,” *Advances in Neural Information Processing Systems*, vol. 32, 2019.
- [41] N. Panigrahy, K. Gopalakrishnan, T. Ilamparithi, and M. Kashinath, “Real-time phasor-EMT hybrid simulation for modern power distribution grids,” in *2016 IEEE International Conference on Power Electronics, Drives and Energy Systems (PEDES)*, pp. 1–6, IEEE, 2016.
- [42] Z. Ren, Y. Tang, and N. Li, “Escaping saddle points in zeroth-order optimization: the power of two-point estimators,” in *International Conference on Machine Learning*, pp. 28914–28975, PMLR, 2023.

TABLE IV
OPTIMAL IBR CONTROL PARAMETERS UNDER SCENARIO 1 DISTURBANCE.

IBR Name	D	M	$K_{i,PLL}$	$K_{p,PLL}$	$K_{i,v}$	$K_{p,v}$	$K_{i,i}$	$K_{p,i}$
IBR1-GFL1	4980.2	–	3182.7	46.4	–	–	43.4	24.5
IBR2-GFL2	5000.0	–	2992.1	88.7	–	–	208.4	61.6
IBR3-GFL3	2015.5	–	2595.9	75.9	–	–	109.4	42.8
IBR4-GFL4	2283.8	–	2547.1	37.1	–	–	288.0	49.0
IBR5-GFL5	4519.3	–	3229.4	55.4	–	–	203.6	37.1
IBR6-GFL6	4535.3	–	2520.4	72.3	–	–	38.6	55.7
IBR7-GFM1	4925.6	26.5	–	–	27.7	29.9	9.5	2.2
IBR8-GFM2	4954.6	17.7	–	–	31.9	5.6	19.4	3.2
IBR9-GFM3	4658.0	26.6	–	–	55.2	5.1	18.0	4.7
IBR10-GFM4	1146.9	30.0	–	–	21.3	40.0	8.0	2.0

TABLE V
OPTIMAL IBR CONTROL PARAMETERS UNDER SCENARIO 2 DISTURBANCE.

IBR Name	D	M	$K_{i,PLL}$	$K_{p,PLL}$	$K_{i,v}$	$K_{p,v}$	$K_{i,i}$	$K_{p,i}$
IBR1-GFL1	1000.0	–	3330.1	37.8	–	–	300	37.3
IBR2-GFL2	1057.1	–	2981.9	58.9	–	–	291.1	62.1
IBR3-GFL3	1206.7	–	3619.9	43.8	–	–	110.7	20.3
IBR4-GFL4	1605.3	–	3197.0	69.8	–	–	250.5	60.2
IBR5-GFL5	1273.9	–	3205.8	61.7	–	–	296.9	65.8
IBR6-GFL6	1086.9	–	2846.0	33.5	–	–	204.6	40.0
IBR7-GFM1	2692.2	10.3	–	–	44.3	5.0	10.4	2.7
IBR8-GFM2	2671.6	8.2	–	–	49.7	5.0	15.8	1.2
IBR9-GFM3	2009.1	13.3	–	–	25.8	18.3	8.1	3.1
IBR10-GFM4	3686.3	10.9	–	–	47.7	19.0	9.8	1.9